Geological Society of America
Special Paper 384
2005

Is Ries crater typical for its size? An analysis based upon old and new geophysical data and numerical modeling

K. Wünnemann*
J.V. Morgan
Department of Earth Science and Engineering, Imperial College London, London SW7 2AZ, UK

H. Jödicke
Institut für Geophysik, Westfälische Wilhelms–Universität Münster, Corrensstraße 24, 48149 Münster, Germany

ABSTRACT

Considering the Ries crater as an example for middle-sized complex impact structures on Earth, we use geophysical data to examine the structure underneath the crater and simulate the formation process by numerical modeling. In contrast to previous investigations, we show by reanalyzing seismic refraction profiles that some clues for structural uplift exist beneath the crater in a range of at least 1 km. We propose that the average P-wave velocity inside the crater is lower than outside the crater from the surface to ~2.2 km depth, but that below this level, the velocity increases beneath the center, presumably due to uplifted basement rocks. In addition, we utilized magnetotelluric depth sounding to investigate the deep electrical structure beneath the crater. Two-dimensional inversion models of the data show anomalously high conductivity beneath the crater. Our best model features a zone of presumably brine-filled fractures in open pore space to a depth of ~2 km. Furthermore, our numerical modeling results for the crater formation are consistent with surface and subsurface observations in the vicinity of the crater. In order to explain the structural differences between similarly sized craters and Ries, we investigate the sensitivity of crater shape and subsurface structure to varying target compositions. We show that for a reasonable range of constitutive material and acoustic fluidization parameters the model calculations produce a large variety of different crater shapes, even for the same amount of impact energy. In contrast to the conventional estimate of crater diameters, our results suggest that Ries crater is comparable in size with the Bosumtwi and Zhamanshin crater. Despite their apparent lack of similarity at first look, Ries and Bosumtwi are closely matched in terms of transient crater size (inner ring), aspect ratio, and structural elements, and we conclude that they both represent typical complex crater structures of the terrestrial impact record for their size range.

Keywords: impact cratering, numerical modeling, Ries, magnetotelluric, Bosumtwi, crater morphology.

*Present address: Lunar and Planetary Science Lab, University of Arizona, 1629 E. University Blvd., Tucson AZ 85721, USA; wunnema@lpl.arizona.edu.

Wünnemann, K., Morgan, J.V., and Jödicke, H., 2005, Is Ries crater typical for its size? An analysis based upon old and new geophysical data and numerical modeling, *in* Kenkmann, T., Hörz, F., and Deutsch, A., eds., Large meteorite impacts III: Geological Society of America Special Paper 384, p. 67–83.

INTRODUCTION

As a basic principle, impact crater morphology is a function of crater size. A major change from simple to complex morphology occurs at a well defined threshold diameter depending on target properties and the given gravity field (e.g., Grieve and Pesonen, 1992). The shape of simple craters is relatively consistent and does not change much with increasing size. In contrast, complex craters show greater variety in morphology and can be roughly subdivided with increasing diameter into (1) central peak craters, (2) peak ring craters, and (3) multi-ring basins (e.g., Melosh, 1989). On Earth it seems to be more difficult to assign a typical crater form to a given crater size than on most other planetary bodies. The lack of consistency between similarly sized terrestrial craters makes it more difficult to understand the dynamics of complex crater formation. A further aggravating circumstance is the fact that most crater structures on Earth are not pristine. Post-impact modifications like erosion and tectonic overprint can prevent, in many cases, an accurate reconstruction of the crater structure and determination of the crater diameter. Thus, it is difficult to define a typical morphology for a given crater size on Earth. In addition, the inhomogeneous composition of the target, which is presumably more complex than on any other planetary body, probably has a fundamental effect on the formation process and might be at least partially responsible for the lack of structural similarity between similarly sized craters.

The investigation of the subsurface of terrestrial impact structures provides important clues to understanding the crater formation process. Thus, it is crucial to know whether a particular crater is a relatively typical example for its size or whether it is a structure where the formation was heavily influenced by local target conditions.

The objective of the present paper is to discuss the structure and morphology of the well preserved and extensively investigated Ries crater in Germany in comparison to other terrestrial craters. Present structural models of the Ries are based on drilling and a variety of geophysical explorations that were mainly carried out in the late 1960s and early 1970s (Angenheister and Pohl, 1969). Here we present a reanalysis of a subset of the seismic refraction data, aimed at investigating the apparent absence of structural uplift beneath the crater center. We also show new magnetotelluric depth soundings that complement the existing data set and provide a model of the electrical resistivity structure deep beneath the crater. Furthermore, we conducted a suite of numerical models of the formation process. Although the field of impact crater modeling has become an important part of modern impact research (Ivanov and Artemieva, 2002), there has been no recent attempt to model the formation of the Ries crater (Stöffler et al., 2001). Computer simulations of the formation process provide important clues to evaluate the influence of varying target compositions on the cratering process and the final crater morphology. For this reason, in our dynamic models of the formation of Ries crater, we tested different assumptions regarding structural composition and material properties of rocks in the vicinity of the crater.

Our analysis is then exemplified by a comparison of Ries with Bosumtwi and Zhamanshin craters, revealing important structural and morphological aspects of middle-sized impact craters.

THE RIES CRATER

The Ries crater is a middle-sized complex crater located ~120 km northwest of Munich (Fig. 1). It was formed ca. 15 Ma (Bolten and Müller, 1969; Gentner et al., 1963) and due to relatively low erosion rates in this area the crater is well preserved. Since 1961, when Shoemaker and Chao (1961) proved its impact origin, the Ries has been intensively investigated, making it one of the best-studied craters on Earth. An excellent review was published by Pohl et al. (1977), but since then no major progress, in terms of the investigation of the deep subsurface structure and understanding the formation of the crater, has been achieved.

The crater is characterized by an almost circular, relatively flat inner basin, 12 km in diameter, which is covered by post-impact lake sediments surrounded by an inner ring. Topographically, this inner ring is only visible as a circular chain of isolated crystalline hills standing ~50 m above the basin. Adjacent to the plains of post-impact lake sediments surrounded by the inner ring, hummocky relief extends to the outer morphological crater rim with an approximate diameter of 24–26 km. This area mainly consists of displaced megablocks up to 1 km in size and is believed to represent a system of concentric normal faults, with the outermost fault referred to as the tectonic or crater rim.

The near-surface structure, to about ~1 km depth, is well investigated. Under the post-impact sediments, with a maximum depth of ~350 m in the central basin (Ernstson, 1974), a 300–400-m-thick suevite layer (a polymict breccia primarily derived from differently shocked basement clasts with cogenetic impact melt clasts and bombs) covers the crystalline basement (Pohl et al., 1977). Suevite deposits up to 200 m in thickness are also found outside the inner ring and are located on the top of the Bunte breccia (derived from near-surface target rocks; cf. Pohl et al., 1977).

The pre-impact stratigraphy of the target is made up of sedimentary deposits, 620–750 m thick, overlying a crystalline basement composed mainly of granites (Pohl et al., 1977). Immediately after the projectile hit this target, a transient crater was formed, and its diameter is believed to have been coincident with the inner ring. The transient cavity would have been roughly one-third of the diameter; e.g., ~4 km deep (Melosh, 1989). Since the crater floor now lies less than ~1 km below the surface in the crater center, some kind of modification process of the transient crater must have taken place. According to the size of the transient cavity, the collapse is most likely associated with structural uplift. However, to date there are no clues in the geophysical data as to the shape and extent of such a structural uplift. In this section, we provide reanalyzed seismic refraction data and new magnetotelluric data to investigate the subsurface beneath the central basin.

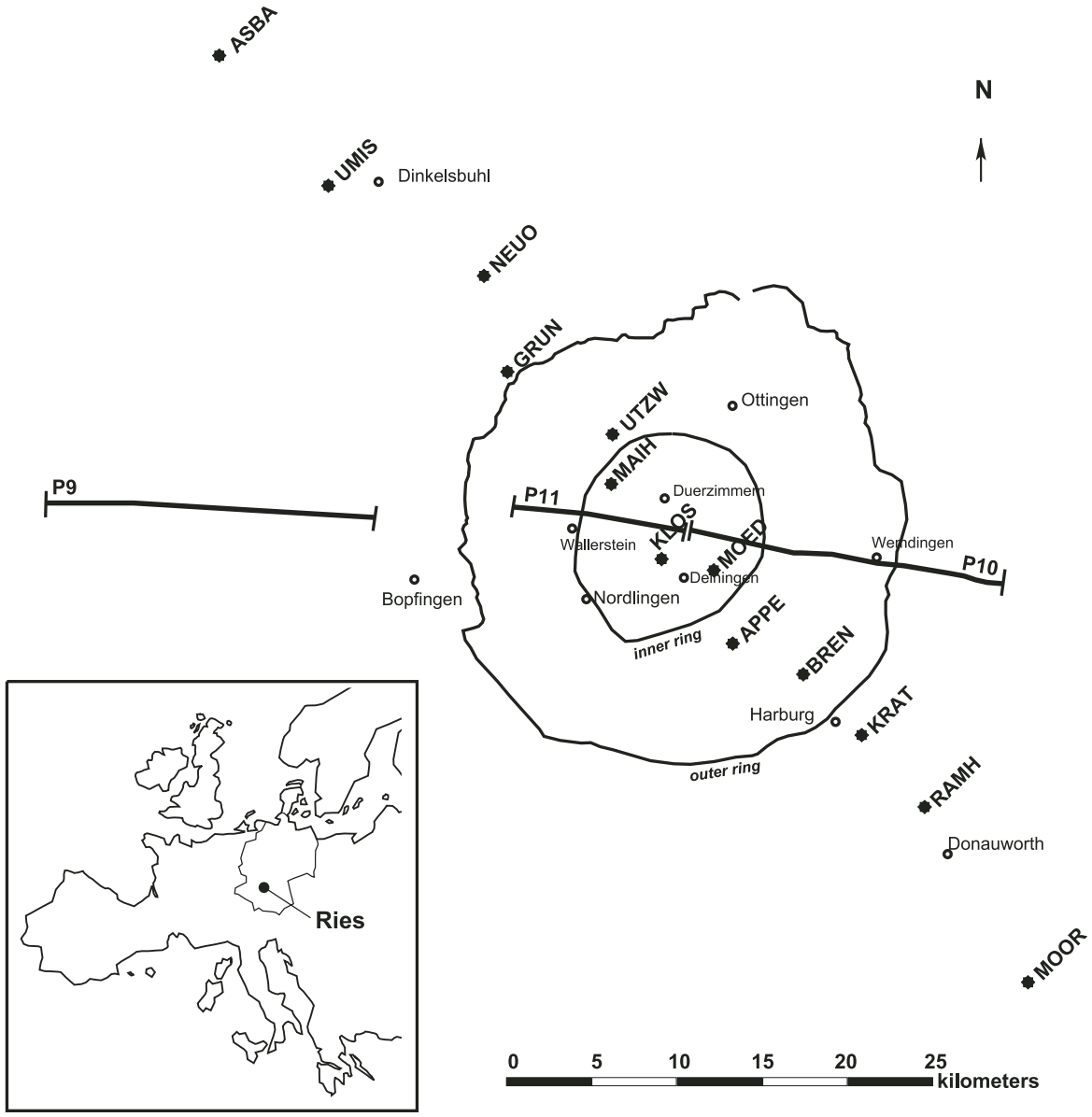

Figure 1. Map of the new magnetotelluric (MT) and the seismic refraction profiles acquired in 1968 (Angenheister and Pohl, 1969) in the Ries crater area. Asterisks mark the positions of MT stations. Bold solid lines indicate the location of the seismic profiles (P9, P10, P11). The circular solid lines display the approximate positions of the inner (crystalline) ring and the outer (tectonic) ridge (Bayerisches Geologisches Landesamt, 1999).

Seismic Refraction Analysis

Several seismic refraction profiles have been acquired across the crater (Angenheister and Pohl, 1969; Pohl and Will, 1974). The authors have concluded that the average velocities inside the crater are lower than those outside, and this low-velocity–zone extends to 3–6 km below the surface (Pohl and Will, 1974; Ernstson and Pohl, 1977). At most complex craters, structural uplift is observed in the crater center and, when not observed in outcrop, can often be detected by its geophysical signature. Structural uplift is typically associated with an increase in seismic velocity, increase in density, and possibly a change in the magnetic or electrical signature (e.g., Pilkington and Grieve, 1992; Karp et al., 2002; Morgan et al., 2002). Thus, a low-velocity–zone in the crater center at Ries apparently indicates an absence of structural uplift at this crater.

All the seismic refraction data are along two-dimensional profiles that are a few tens of kilometers long (Fig. 1), and most consist of a single shot at one end that is recorded at receivers spaced a few kilometers apart. To be able to constrain lateral changes in velocity, multiple shots are required into multiple receivers, and velocity resolution is directly related to the shot

or receiver spacing, whichever is the largest (Zelt, 1998). Hence, single shot profiles provide no lateral resolution. Profile 11 (P11 in Fig. 1) is reversed—a shot was fired at each end. This is the only profile that has crossing ray paths, and thus the only profile with any lateral resolution—albeit quite limited. Profiles 9 and 10 were acquired in an expanding spread configuration, in which a number of single shots were recorded on single receivers, with the shot and receiver being moved to maintain a constant midpoint. In expanding spread profiles, there are no crossing ray paths and, because of this, they are conventionally modeled with a one-dimensional interpretation (e.g., Fowler et al., 1989). From the experimental geometries of the current suite of seismic refraction data, it is clear that lateral changes in velocity cannot be well constrained. Given the limitations of these data, we have adopted the most objective approach—that is to find the best-fit one-dimensional velocity model that fits the data. Here we reanalyze the best of these data: refraction profiles 9, 10, and 11. Profile 9 is entirely outside the crater rim, profile 10 mostly inside the crater rim, and profile 11 entirely inside the crater rim (see Fig. 1).

P-wave velocity usually increases with depth, and upper crustal continental rocks typically have velocities of between 6.0 and 6.2 km s^{-1} (e.g., Christensen and Mooney, 1995). The basement rocks at Ries are granitic; fully compacted granites also have velocities of between 6.0 and 6.2 km s^{-1} (Birch, 1961). With this in mind, we have replotted the refraction data with a reduction velocity of 6 km s^{-1} (Fig. 2). In such plots, arrivals with an apparent velocity of 6 km s^{-1} appear as horizontal lines and are easy to identify, and any difference in the appearance of refractions from layers with this velocity are easy to spot. The vertical lines in these plots are picked first-arrival travel times. The picks for profiles 9 and 10 are taken directly from Pohl and Will (1974). Profile 11 data is directly from Angenheister and Pohl (1969); these data show a low signal to noise ratio, and first-arrivals were not easy to pick.

As mentioned above, we have obtained the best-fit one dimensional velocity structure for each profile (Figs. 2 and 3). The program RAYINVR has been used to ray-trace the data (Zelt and Smith, 1992), and the straight lines through the arrivals in Figure 2 are the calculated travel times. Profiles 9 and 10 are both very simple and easy to interpret as the picked arrivals are clearly aligned along three straight lines with different apparent velocities (V_a in Fig. 2). These plots suggest a subsurface consisting of three layers, with the velocity of the top two layers being higher for profile 9 (3.3 and 5.35 km s^{-1}) than profile 10 (2.0 and 4.2 km s^{-1}; Fig. 3). Profile 11 shows more lateral variation, and the best-fit straight lines have a larger misfit. This suggests there are either lateral changes in velocity across this profile or some of the boundaries between individual layers are dipping. However, the most striking difference between the profiles inside and outside the crater is the point at which the phase with an apparent velocity of 6 km s^{-1} becomes a first arrival. Outside the crater (Fig. 2A), this first occurs at ~23 km, whereas inside the crater, it occurs between 6 and 8 km (Fig. 2B–D). This observation strongly suggests that the depth at which velocities of 6 km s^{-1}

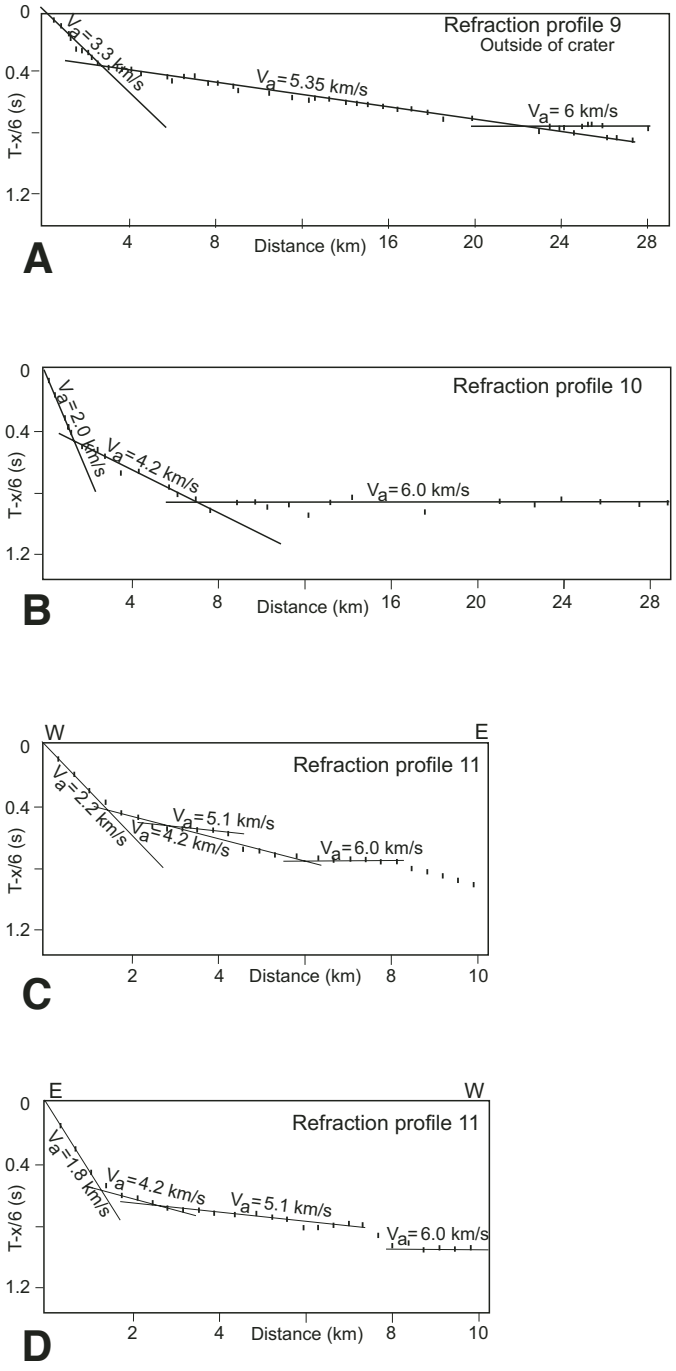

Figure 2. Traveltime plots of seismic refraction data along (A) profile 9, (B) profile 10, and (C) profile 11, with a shot at the western end of profile, and (D) profile 11, with a shot at the eastern end of profile. The horizontal scale is the distance from shot to receiver—note the different scaling for the two upper and lower profiles. The vertical scale is the time taken to travel from shot to receiver, plotted in reduced time, which equals the true arrival time (TAT) minus distance (X) divided by 6 ([TAT – X]/6). A subset (~30%) of the picked first-arrival traveltimes is plotted as tick marks. When consecutive arrival times align along a straight line, the P-waves are traveling at a constant apparent velocity (V_a). Straight lines are calculated first-arrival traveltimes for the one-dimensional velocity models shown in Figure 3. The V_a values are apparent P-wave velocities of picked arrivals.

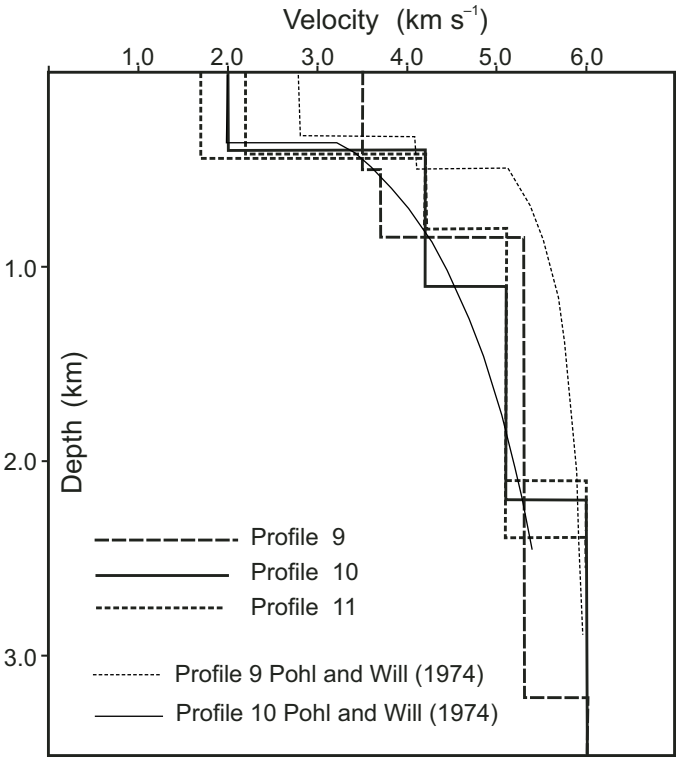

Figure 3. P-wave velocity/depth profiles determined from modeling of arrivals shown in Figure 2 for profiles 9, 10, and 11. For comparison, velocity models for profiles 9 and 10 from Pohl and Will (1974) are also displayed.

first occur is deeper outside the crater than inside the crater. In our one-dimensional interpretation of the data, velocities of 6 km s^{-1} are reached between 2.1 and 2.4 km depth for the three profiles inside the crater, whereas outside the crater this velocity boundary is at ~3.2 km (Fig. 3). This depth is in agreement with a seismic refraction model presented by Pohl et al. (1977), in which the 6 km s^{-1} velocity contour is at ~3.1 km depth to the southeast, northeast, and northwest of the crater.

From our analyses of the refraction data, we suggest that the average velocity inside the crater is lower than outside the crater from the surface to ~2.2 km depth. Moreover, the apparent elevation of the 6 km s^{-1} velocity boundary by ~1 km within the crater center supports the proposal that there might be structural uplift here. We acknowledge that it is possible to construct other velocity models with dipping interfaces and/or with lateral velocity changes that show no structural uplift (e.g., Ernstson and Pohl, 1977) and that these might fit the data equally as well. However, such lateral changes are not well constrained by the current data set. The linearity of the arrivals in refraction profiles 9 and 10 (Fig. 2A and 2B) do not suggest strong lateral changes in velocity, although we recognize that they could easily be generated from a velocity model with one or more dipping interfaces. Taking all these factors into consideration, we conclude that the seismic refraction data are consistent with a structural uplift of ~1 km at the Ries crater.

Magnetotelluric Investigation of the Deep Subsurface of the Crater

In order to further investigate the deep structure beneath the Ries crater, the distribution of electrical conductivity was studied by means of magnetotelluric (MT) measurements during two short field campaigns in 1999 and 2000. Utilizing the induction effect of natural variations in Earth's magnetic field for electromagnetic deep sounding, the MT method is particularly capable of detecting highly conductive structures in the deep subsurface. Within the generally highly resistive upper crustal environment of the Moldanubian belt (ERCEUGT-Group, 1992) such structures would be readily visible, allowing an estimate of the extension of porous or fractured zones to depth. An early MT study by Haak et al. (1977) confirmed the existence of highly conductive lake deposits inside the crater, but the deep electrical conductivity structure beneath the crater was not analyzed. Other MT studies of impact structures in Sweden (Siljan; Zhang et al., 1988) and Canada (Charlevoix; Mareschal and Chouteau, 1990) revealed zones of increased electrical conductivity below the craters, indicating the existence of fractures that might enable fluid circulation at depth. At the Ries crater, we attempted to find constraints from electrical parameters that could support the presence of basement uplift or deep reaching fractures, as favored by Pohl et al. (1977).

The natural time-varying electric and magnetic fields were measured at 13 MT sites along a NW-SE–trending profile (Fig. 1); i.e., perpendicular to the geological strike of the Moldanubian gross structure (cf. Haak et al., 1977). The entire length of the profile extends over 73 km, with an average spacing between the measurement points of 10 km outside the crater and 2–5 km between the outer and the inner ring. The MT data, covering a period range of 0.25–4096 s, were recorded in three bands at sampling rates of 16 Hz, 2 s, and 32 s. Due to the high level of cultural noise, typical of populated areas, the data quality of the short period band was too low at some sites to be used for modeling, especially inside the crater structure.

To obtain magnetotelluric transfer functions, as displayed in Figure 4 in the form of resistivity and phase curves, standard MT data processing was applied (cf. Jording et al., 2000). It includes statistical frequency analysis methods as well as decomposition procedures in order to test for static shift effects. Considering the circular crater structure, a three-dimensional MT study would have been appropriate; however, the dimensionality analysis of the data gave skewness values <0.3 for all sites and periods, which means that two-dimensional modeling may be applied as an approximation (e.g., Bahr, 1991). Furthermore, due to the lack of noticeable static shift effects, it was not necessary to correct for them. The coordinate systems of all individual data sets were rotated by the same −45° angle into the system parallel to the large-scale geologic strike approximating the profile direction. Hereby, the E- and the

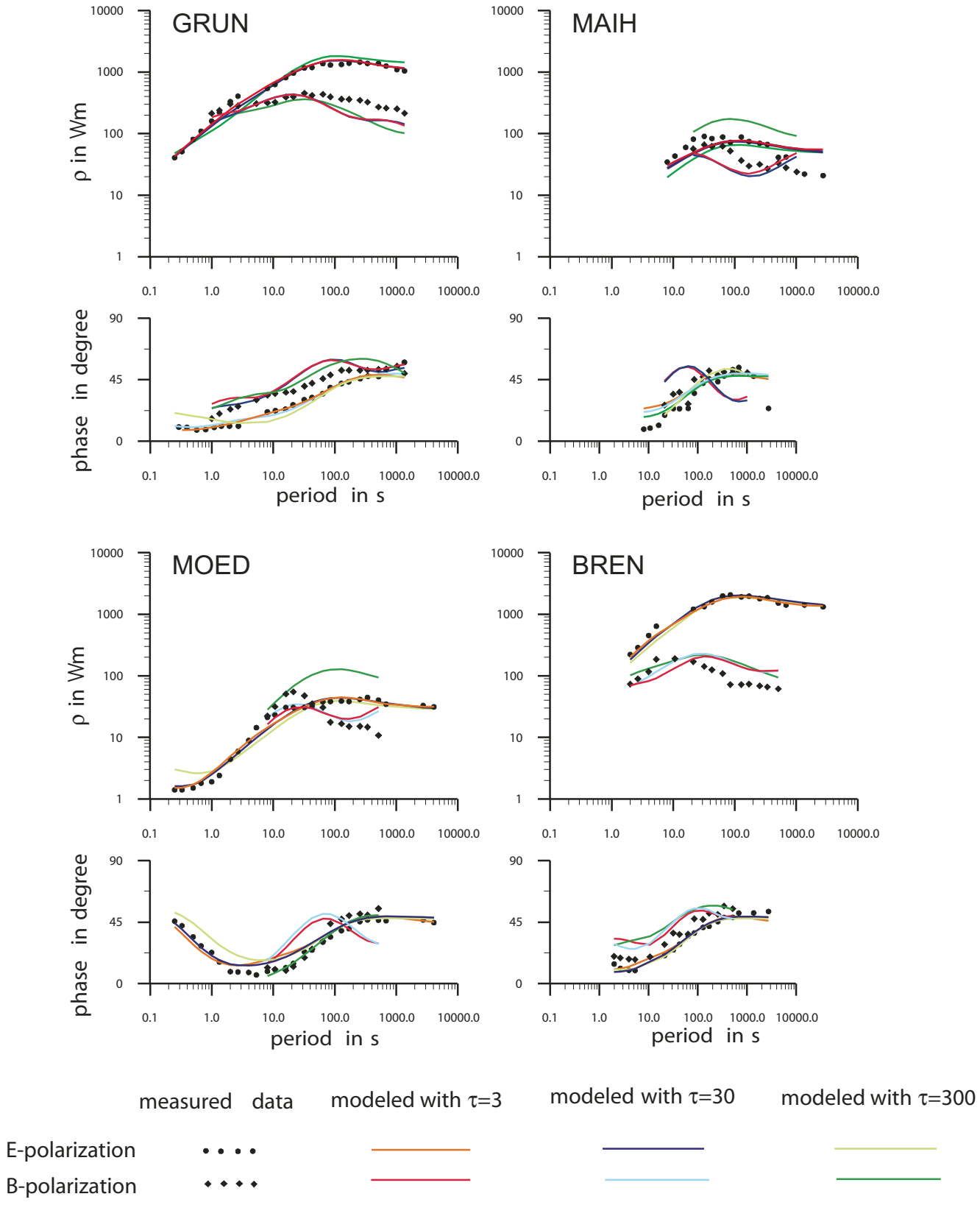

Figure 4. Examples of 4 magnetotelluric apparent resisitivity (ρ) and phase curves. Each chart shows a comparison of measured data (tick marks) and curves obtained from MT-models I (τ = 3), II (τ = 30), and III (τ = 300) (see Fig. 5). For the location of the stations (GRUN, MAIH, MOED and BREN) see Figure 1.

B-polarization modes were determined, at least roughly, as needed for two-dimensional modeling (cf., Jording et al., 2000).

Using the inversion algorithm by Mackie et al. (1997), resistivity and phase data of the E- and the B-polarization modes were inverted simultaneously. Special emphasis was placed on the analysis of the influence of the regularization parameter, τ, which enables us to find models varying from best fit of the local sites (small τ) to lateral smoothing of the resistivity structure as a whole (large τ). As a result of our calculations, three models (I, II, III) with different values of τ (3, 30, 300) are presented in Figure 5. The corresponding model fits of four selected sites from the inner crater range are displayed in Figure 4. Taking the limitations of the two-dimensional approximation into account, the overall misfit of the models (root mean square [rms]-error) is reasonable (Fig. 5). The overall fit is small for the models with small or medium τ (rms = 7.49, 7.23) and somewhat larger for the model with large τ (rms = 11.27). Influenced by the outer two-dimensional effect of the gross geological structure, the data fit at the sites GRUN and BREN near the outer crater ring is remarkably better than for the central, possibly three-dimensionally influenced sites MAIH and MOED. The main effect of the conductivity anomaly is clearly evidenced by relatively low apparent resistivity values of 10–100 Ωm in the inner ring compared to 100–1000 Ωm near or outside the outer rim (Fig. 4).

Independently of τ, all models show a near surface (< ~1 km) high-conductivity zone (3–10 Ωm) within the crater, centered at the position of its inner ring (Fig. 5). These resistivity values are in good agreement with the resistivity values of the lake sediments (~1–4 Ωm) and the suevite layer (~10 Ωm), known from borehole measurements in the deep drill hole Forschungsbohrung Nördlingen (Ernstson and Pohl, 1974) and by geoelectric deep soundings inside the inner ring (Ernstson, 1974; Blohm et al., 1977). At larger depths, another conductive structure appears in models I and II, right below the crater center, reaching to depths of 4 and 6 km, respectively (Fig. 5). This structure is clearly separated from the surface layer, whereas the equivalent structure in model III is connected with the surface layer, reaching a maximum depth of ~2 km only.

Strikingly, in all three models, the resulting resistivity minimum (or maximum of the electrical conductivity) at larger depths is shifted from the morphological crater center toward the northwest by 2–3 km (note the dashed lines indicating the inner ring and outer rim in Fig. 5). This shifted position was also found for the minimum Bouguer anomaly related to the Ries crater (Jung and Schaaf, 1967; Kahle, 1969) as shown by the values of the uncorrected Bouguer anomaly along the MT profile extracted from the Bouguer gravity map of Jung and Schaaf (1967) (top of Fig. 5). Any convincing explanation of this discrepancy is missing so far. The first idea, namely that it might be caused by an oblique northwest directed impact, can be ruled out due to the distribution of ejecta (tektites). The moldavite (tektite) strewn field extends from the crater center east–northeastward, and according to earlier modeling (Artemieva et al., 2002) it is most likely that the impact was oblique coming from a west-southwest direction.

Various attempts have been made to model the gravity anomaly of the Ries (Jung and Schaaf, 1967; Kahle, 1969, 1970), the most satisfactory of which is the refined model of Kahle (1969). This model explains the crater-related gravity minimum by means of a series of four cylindrical layers (I–IV) with decreasing density contrasts (≥−0.49, −0.25, −0.20, −0.15 g/cm^3) and radii (11.0, 5.0, 3.5, 2.0 km) and thicknesses of 0.5 km each (Fig. 6). The geometric dimensions of this model are in good agreement with the conductivity distribution of model III.

A direct comparison in model III (Fig. 6) between density data and conductivity, both depending mainly on porosity, is suitable at least for larger depths, where a simple power law (Archie's formula) may be applied to roughly estimate the porosity needed to explain the observed conductivity. The resulting values, between 10% and 20% for the suevite layer and the uppermost part of the basement, assuming high saline water (0.3–1 Ωm) as supposed by Blohm et al. (1977), are also generally in good agreement with the results of the density model. Further support for model III comes from purely magnetotelluric arguments. In model III, the phase fits of the inner crater sites are superior to those of models I and II in spite of their smaller rms errors (Fig. 4). The phase fit is more valuable because phases are less distorted by static shift or biased by correlated noise effects than are the apparent resistivity values. Based on these arguments, we may favor model III, although we have to be aware that all models (I–III) represent more or less equivalent solutions. The choice of model III would exclude deep-reaching fractures below the crater, in good agreement with the seismic model, if the resistivity increase at 2–3 km depth is interpreted as a transition to dense and resistive basement rocks. On the contrary, models I and II would indicate the existence of a fractured zone underneath the crater expanding to depths of 4 or 6 km, respectively.

NUMERICAL MODELING OF CRATER FORMATION

We utilized numerical modeling to simulate the formation of Ries crater and to investigate the influence of varying target composition on the formation process for similarly sized impact structures in general. We used the well-known SALE-3MAT (Simplified Arbitrary Lagrangian-Eulerian 3 Material) hydrocode (Amsden et al., 1980), including some major changes to the original version (e.g., stress- and multi-material-extension; Ivanov et al. 1997; Wünnemann and Lange, 2002) to compute the entire formation process. All calculations begin with the first contact of the impactor and last until the main dynamic motions have ceased. The impact velocity is 18 km s^{-1}, consistent with the mean impact velocity on Earth (O'Keefe and Ahrens, 1994). The target is composed of granite basement covered by an 800-m-thick sediment layer. The thermodynamic behavior of the different materials is calculated by the Tillotson equation of state (EOS; Tillotson, 1962) using material properties of a wet tuff for the sediments and by the analytical equation of state (ANEOS; Thompson and Lauson, 1972) for the granitic basement. Apart from the thermodynamics, the elasto-plastic response of the

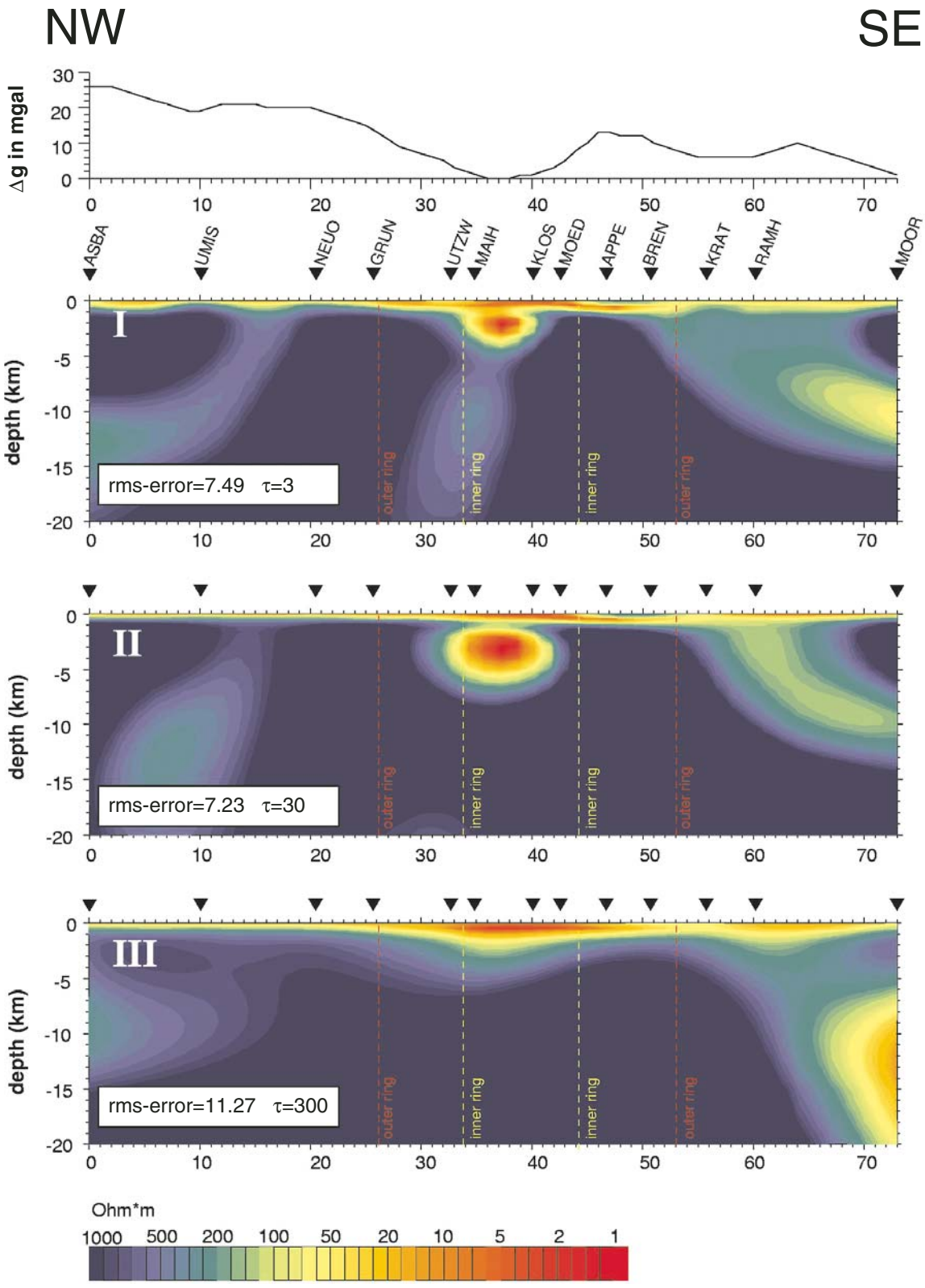

Figure 5. Two-dimensional MT-models (I–III) after Mackie et al. (1997) for different regularization parameters τ, with overall root mean square error (rms-error), compared with the Bouguer anomaly along the MT profile (top; cf. Fig. 1), extracted from the Bouguer gravity map (Jung and Schaaf, 1967). For the location of stations (ASBA, UMIS, NEUO, GRUN, UTZW, MAIH, KLOS, MOED, APPE, BREN, KRAT, RAMH, MOOR) see map in Figure 1.

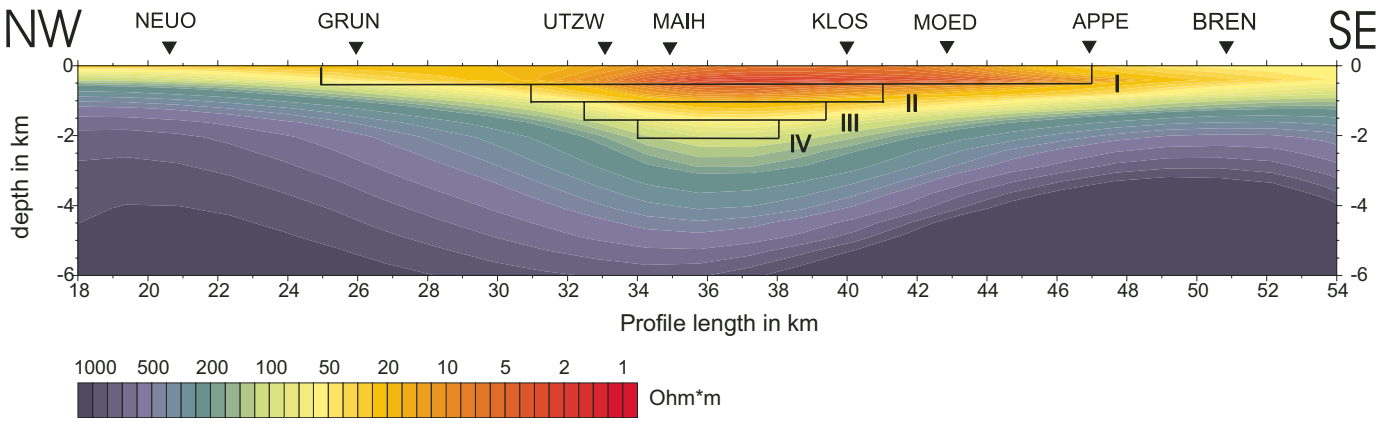

Figure 6. Comparison between MT model III (Fig. 5) and the gravity model consisting of cylindrical layers (I–IV), redrawn after Kahle (1969) along the MT profile (cf. Fig. 1). For the location of stations (NEUO, GRUN, UTZW, MAIH, KLOS, MOED, APPE, BREN) see map in Figure 1.

material to a given stress field is crucial for the collapse of the transient cavity and the formation of the final crater shape. We utilized standard constitutive models to describe the strength properties of rocks that are exposed to strong deformations (e.g., Ivanov et al., 1997). In these models, the yield strength Y is a function of pressure P and temperature T, and is mainly controlled by the coefficient of internal friction ϕ and the cohesion C. In addition, an acoustic fluidization model was used to explain the temporary fluid-like behavior of rocks in the vicinity of the crater (Melosh, 1979). The behavior of acoustically fluidized matter is mainly determined by the viscosity η and the decay time T_{dec}, which describes how long the viscous state of the material lasts until the vibration (acoustic wave field) is damped down. Both parameters, η and T_{dec}, are strongly linked with the fragmentation state (fragment size) of the rocks beneath the structure.

For a full description of the rheology and especially of the acoustic fluidization model utilized in the present study, we refer to Wünnemann and Ivanov (2003), Melosh and Ivanov (1999), and Melosh (1979). The covered ranges for all material parameters as well as all important model specifications are summarized in Tables 1 and 2.

Dynamic Model of Ries Crater Formation

The numerical model that best matches the present crater morphometry is shown in Figure 7. Snapshots at different stages

TABLE 1. PARAMETERS USED IN THE NUMERICAL MODELS OF THE RIES

Parameters	Values
Impactor:	
Diameter	1100 m
Impact velocity	18 km s^{-1}
Material/EOS	Granite, ANEOS
Top layer:	
Material/EOS	Wet tuff properties/Tillotson (1962)
Cohesion C_S	0, 10 MPa
Dry friction coefficient ϕ_S	0.5, 0.9
Thickness I	800 m, 2000 m
Basement:	
Material/EOS	Granite, ANEOS
Cohesion C_B	10 MPa
Dry friction coefficient ϕ_B	0.9
Model set-up:	
Number of cells nx × ny (radial, vertical)	350 × 350 cells
Number of extended cells top, right, bottom	40, 70, 70
Spatial increment (high resolution area)	50 m

Note: EOS—equation of state; ANEOS—analytical equation of state.

TABLE 2. ACOUSTIC FLUIDIZATION PARAMETERS USED IN MODELS A, B, C, AND D (FIGS. 9 AND 10)

	Acoustic fluidization parameters	
Model description	Viscosity η	Decay time T_{dec}
(A) Best-fit model (Fig. 9)	1.50 GPa s	33.0 s
(B) Wünnemann and Ivanov (2003) (Fig. 10B)	0.70 GPa s	16.5 s
(C) Ivanov and Artemieva (2002), Bosumtwi model (slightly modified), (Fig. 10C)	0.07 GPa s	11.0 s
(D) As (3), but longer lasting vibration (compare to Chicxulub morphology, Collins et al. [2002]) (Fig. 10D)	0.07 GPa s	22.0 s

of the cratering process illustrate the crater formation. In each frame the left-hand side shows tracers arranged in horizontal layers that depict the stratigraphy and the uplift of the target rocks due to the collapse of the transient cavity. On the right-hand side, the density distribution of the rocks is indicated. The change in density between the overlying rocks and the crystalline basement is pronounced. In the model (Fig. 7), the inner ring has a diameter of ~12 km and is formed from uplifted and outwardly displaced basements rocks. The megablock zone between the inner ring and outer rim, which is basically characterized by concentrically faulted separate blocks, is represented in the model by a continuously inclined overlying layer, which extends to a radial distance of ca. 12 km. The shape of the modeled crater is generally consistent with the observed crater morphometry. In addition, the thermodynamic history and the displacement of rocks in the vicinity of the impact structure are illustrated in Figure 8. On the left-hand side of this figure, the maximum pressure each tracer particle has experienced throughout the impact process is shown with respect to the final position of the tracer. Peak pressures above 46 and 56 GPa usually cause incipient and complete melting, respectively, in granite after release from shock pressure (Pierazzo et al., 1997). Thus, the top layer inside the inner crater is composed of melt-rich material that is roughly coincident with the suevite layer in the Ries crater. The right side illustrates the distance traveled by each tracer relative to its initial location, where all distances are scaled between 0 and 1. The total displacement is accumulated along the path a tracer follows throughout the entire cratering process (not to be mistaken with the distance between the initial and the final position of a tracer). A hemispherical zone of strong tracer displacement (>0.25 of maximum displacement) can be identified to a depth of ~6 km (Fig. 8). It is likely that rocks inside this area are exposed to strong deformations causing brittle fracturing. The upper 2 km are intensively fractured (completely damaged) according to the large magnitude of displacement (>0.75 of maximum displacement). Below this level, down to a depth of 6 km, fracturing is less pronounced (displacement: 0.25–0.75). The rocks in this region have experienced shock pressures <10 GPa (Fig. 7), which is a typical range where fracturing by release from shock pressure occurs (e.g., Grieve et al., 1996). Our best-supported conductivity model, based on magnetotelluric measurements (III, Figure 5), is consistent with this assumption concerning the extent of the fragmentation zone. The tracer layers on the left-hand side in Figure 7 indicate that rocks are uplifted by 1.5–2 km within the crater center, which is roughly in agreement with the stratigraphic uplift of at least 1 km derived from the analyses of the refraction data (Fig. 2 and 3). Therefore, the model presented in Figure 7 agrees in both crater morphometry and interior crater structure with the observations at the Ries crater.

Influence of Different Target Properties on Crater Morphology

The large-scale rheology of rocks is complex and cannot be reproduced in the laboratory with measurements on small samples. Even the same kind of rock can exhibit different rheological properties, especially in terms of cohesion and internal friction, depending on its exact mineralogical composition and also on its thermodynamic and mechanical history. Different constitutive properties as well as varying compositions of different kinds of target rocks may have a strong influence on the formation process and could well be responsible for the lack of structural similarities of similarly sized craters on Earth.

Although we have included a sedimentary layer (wet tuff EOS parameters in Table 1) covering the crystalline basement (granite EOS parameters) in the calculations yielding the best-fit results, shown in A-1 in Figure 9, the strength properties for both materials are the same. We used a cohesion of 10 MPa and a coefficient of internal friction of 0.9 in both layers. Although these parameters suggest a higher strength than expected for sediments, they lead to the best agreement with the observed morphology, in particular the rise of the inner ring above the pre-impact surface level. Usually, sediments are assumed to exhibit much weaker strength properties (smaller internal friction coefficient and smaller cohesion) than basement rocks. Furthermore, assuming cohesive strength in both layers (sediments and basement) contradicts the usual assumption that rocks in the vicinity of the crater are heavily fractured, possessing no or very little cohesive strength. Much weaker strength properties for the sediment layer ($C_S = 0$, $\phi_S = 0.5$) result in the crater morphology shown in A-2 in Figure 9. While the upper layer slumps further inward, the crystalline inner ring collapses further outward above

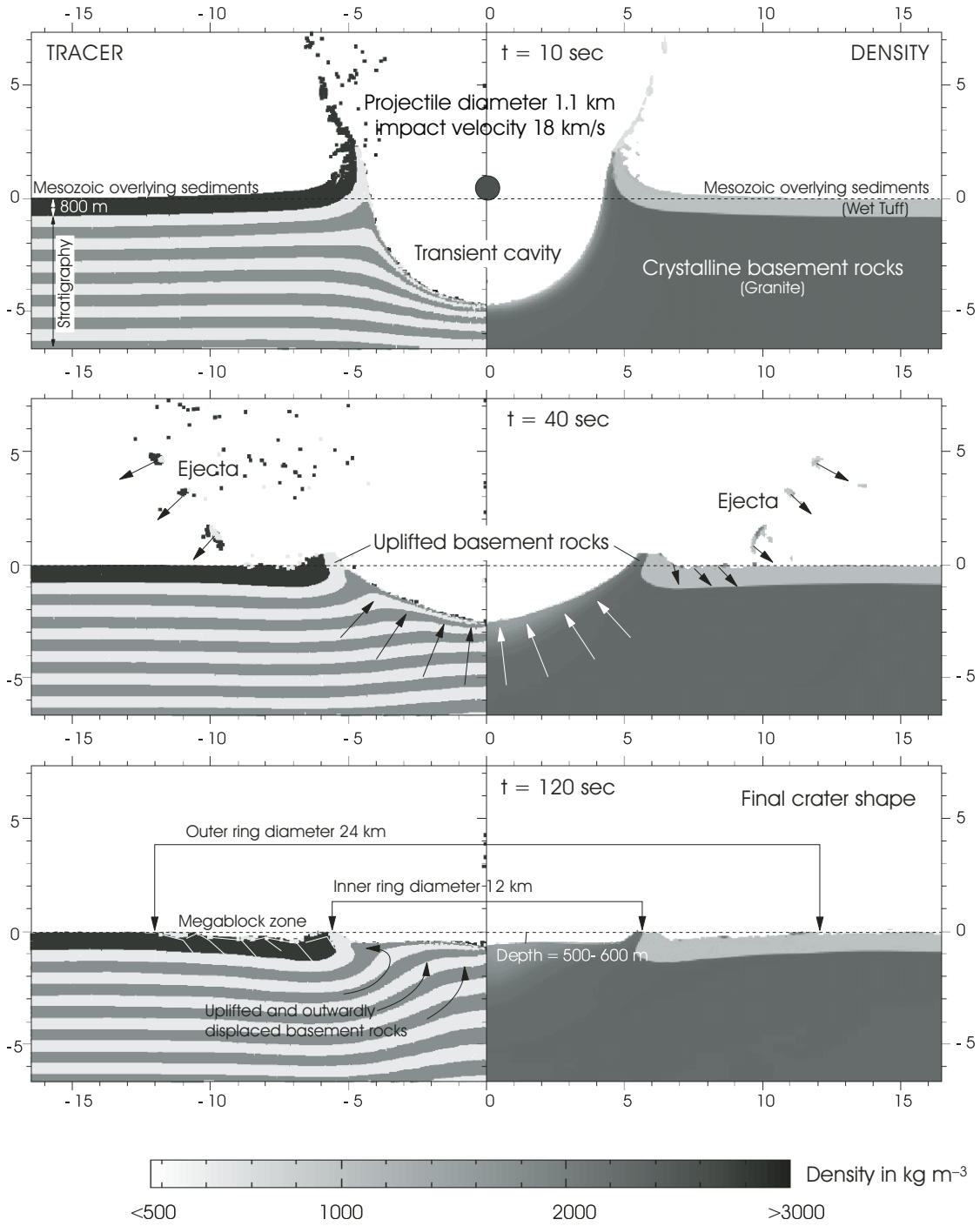

Figure 7. Series of snapshots of our best-fit model A illustrating the formation process of the Ries crater (see Tables 1 and 2 for specific model parameters). All distances are given in km. The left frame shows tracer particles arranged in horizontal layers to illustrate the stratigraphic uplift. The uppermost layer (black) represents the sediment layer. On the right frame, the density distribution is shown.

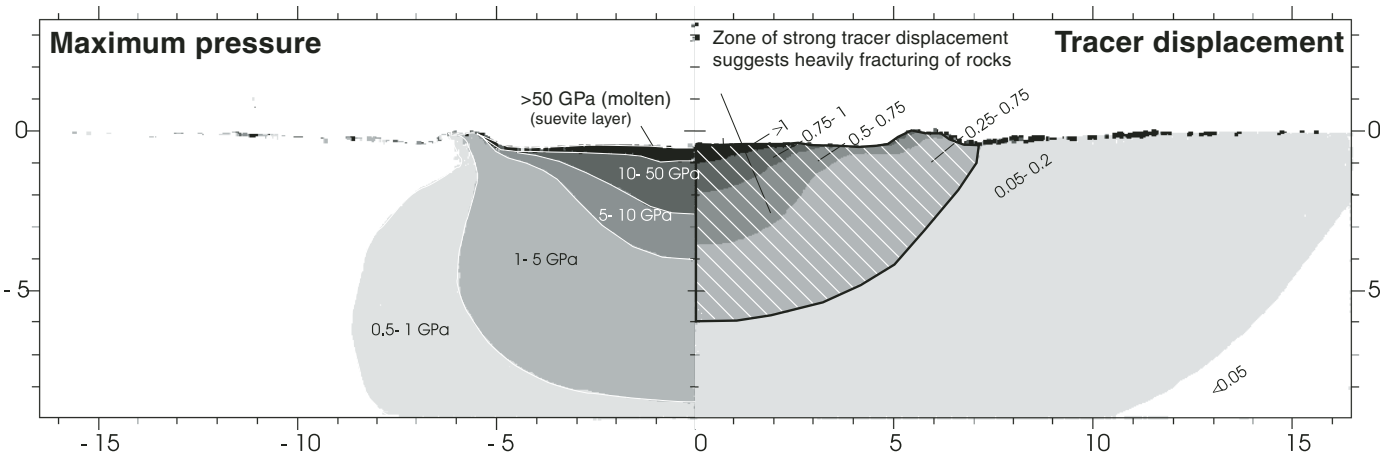

Figure 8. Final crater shape of model A (compare to Fig. 7). The left frame indicates the maximum pressure each tracer has experienced during the crater formation. The right frame shows the accumulated distance traveled by the tracers from their initial positions (not to be mistaken with distance between initial and final position; see text for further explanation). All displacement distances are scaled between 0 and 1.

the sediments (bidirectional material movements), giving rise to an inversion of the stratigraphy. The overall morphology appears to be flatter, featuring less distinct topographic elements than in the upper model (A-1). For instance, the distinct topographic elevation of the inner ring in model A-1 does not appear in model A-2. Finally the influence of increasing thickness (l = 2 km) of the soft (C_S = 0, ϕ_S = 0.5) sediment layer on the top of a crystalline basement is demonstrated in A-3 in Figure 9. No bedrock is uplifted to the surface, although a kind of a dome structure is formed beneath the upper layer. Sediments slump into the crater cavity and over the central dome, covering any topographic evidence of a peak or inner ring structure. The area where the final surface level is below the pre-impact level extends much further outward than in A-1 or A-2, so the final crater structure appears somewhat larger.

Our numerical simulations (Fig. 9) demonstrate, in agreement with other studies (e.g., Shuvalov et al., 2002), that varying mechanical properties in different material layers can dramatically affect the morphology of the final crater structure. The weaker the material in the upper layers, the smoother the resulting crater morphology, and topographic elements are less distinct. However, the structure beneath the crater does not change significantly with variations in the near-surface material strength.

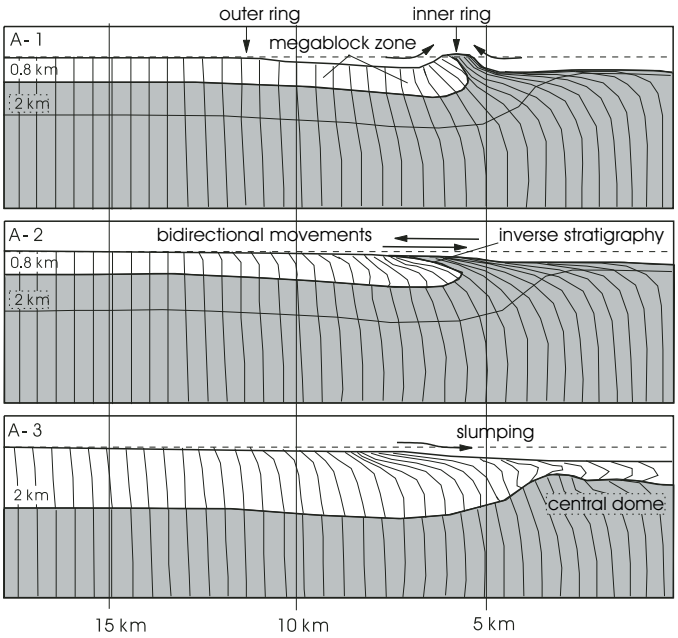

Figure 9. Comparison of the final crater shape of three models utilizing different strength properties and spatial extensions of the upper (sedimentary) layer. Model A-1: l = 0.8 km, C_S = 10 MPa, ϕ_S = 0.9; Model A-2: l = 0.8 km, C_S = 0 MPa, ϕ_S = 0.5; Model A-3: l = 2 km, C_S = 0 MPa, ϕ_S = 0.5 (see text for an explanation of the variables; see also Tables 1 and 2). All models were carried out using the same impact energy.

Influence of Acoustic Fluidization Parameters on Final Crater Form

Although investigations of the subsurface of crater structures confirm the existence of a fragmentation zone deep beneath the surface, the actual state of the rocks in terms of fragment size is unknown and can only be estimated. Unfortunately, the parameters utilized in the acoustic fluidization model, such as the viscosity η and the decay time T_{dec} of the vibration, are particularly dependent on these rock properties in the vicinity of the crater. Different estimates of the mean fragment size have been proposed, mainly by adjusting the parameter choice so the models fit best with the observations (Wünnemann and Ivanov, 2003; Ivanov and Artemieva, 2002). Apart from modeling studies, deep drilling of the 40 km Puchezh-Katunki structure reveals

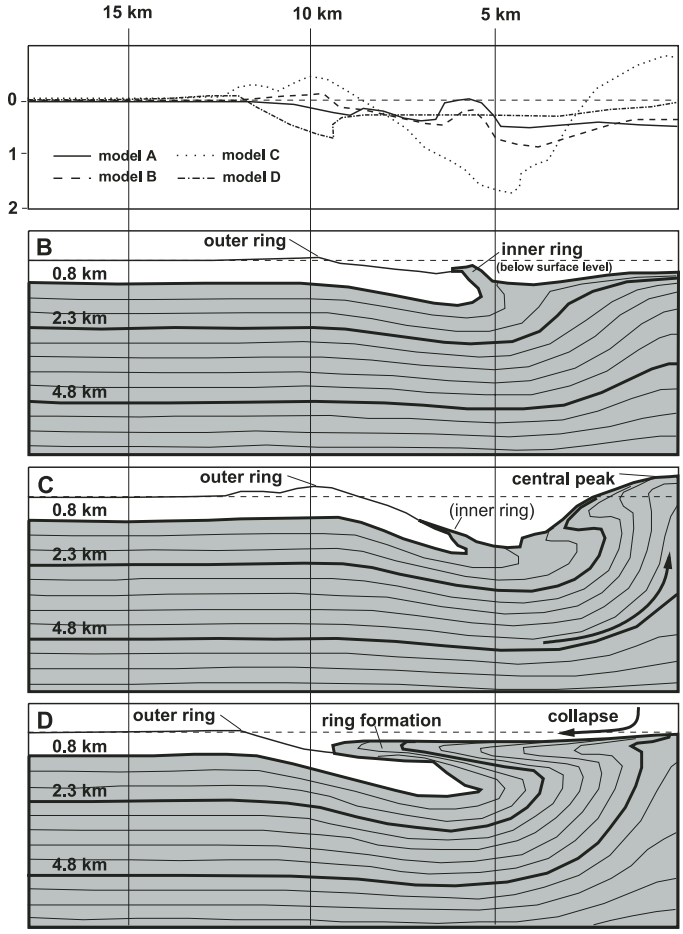

Figure 10. Comparison of the final crater shape of three models (B, C, D) utilizing different acoustic fluidization parameters (η, T_{dec}; see Table. 2). The strength properties correspond to the values in model A-1 (C_S = 10 MPa, ϕ_S = 0.9). The uppermost frame shows a diagram comparing the final crater topography of all models in this figure (model B, C, D) and from Figure 7 (model A-1). All models were carried out using the same impact energy.

a system of blocks with an average size of ~100 m (Ivanov et al., 1996). The investigation of the size of ejected fragments (Kocharyan et al., 1996) and the variety of parameter choices in numerical models suggests that fragment size is a function of crater diameter. In larger crater structures, the block size is assumed to be much larger than in smaller craters and, therefore, the acoustically fluidized state lasts longer and the rock fragments behave more viscously. As Wünnemann and Ivanov (2003) show, it is possible to scale η and T_{dec} as a linear function of projectile size to reproduce the observed depth-diameter dependence of impact craters. However, the parameter choice for similarly sized craters is not unique. More or less similar results arise from a low viscosity and short decay time as from a high viscosity with a longer lasting vibration. In order to investigate the sensitivity of the crater shape to the choice of η and T_{dec}, we have modeled the final crater morphology for a broad range of plausible parameters for Ries-sized craters. The applied values are displayed in Table 2 and compared with those proposed in other numerical modeling studies. Nearly identical results to our best-fit model (model A: η = 1.5 GPa s, T_{dec} = 33 s) arise if the values proposed by Wünnemann and Ivanov (2003) are applied (η = 0.7 GPa s and T_{dec} = 16.5 s; Fig. 10B) using the suggested scaling law for acoustic fluidization parameters as a function of projectile size. Only the crater floor inside the inner ring is slightly more uplifted and is convex in shape. Moreover, the inner ring no longer rises above the pre-impact surface level. Utilizing parameters close to the range used in the Bosumtwi crater model (Ivanov and Artemieva, 2002; Table 2 herein) results in a final crater shape that differs clearly from the previous models, featuring a well defined central peak (Fig. 10C). In addition, the topographic evidence for the crystalline rim of the transient cavity (inner ring) is missing in this model, and the size of the crater structure is determined clearly by the outer (tectonic) crater rim at ~10 km radius. Because the Bosumtwi crater is smaller than the Ries, η was chosen to be twice as large and T_{dec} less than half, following the model by Ivanov and Artemieva (2002). Assuming an even longer vibration time (twice as long) with the same η yields a final crater shape in which the central peak is collapsed (Fig. 10D). The collapse gives rise to the formation of a peak ring at ~9 km, and the outer edge of the crater extends to a diameter of ~12 km. This model is similar to that proposed for the Chicxulub crater by Collins et al. (2002).

The presented results clarify that the final crater morphology is very sensitive to the assumed parameter choice of the acoustic fluidization model. The values proposed by Wünnemann and Ivanov (2003) might be the most reliable ones, because they have been verified over a broad range of crater sizes to be consistent with observed depth/diameter ratios. However, the general simplicity of the model (acoustic fluidization parameters are presumed to be a function of distance to the point of impact) and the lack of information about fragment sizes does not allow more precise statements. Furthermore, the rim of the final crater structure appears at different radii in all four models (Figs. 9 and 10). While models A and B show clear evidence for an inner ring structure coincident with the size of the transient cavity, models C and D are characterized by a more distinct tectonic crater rim and are lacking any topographic clues of the former transient cavity.

DIFFERENCES IN SUBSURFACE STRUCTURE AND SHAPE OF SIMILARLY SIZED CRATERS ON EARTH

When we examine the crater morphology and subsurface structure of the Ries and similarly sized terrestrial craters, we see surprising dissimilarities in terms of crater morphometry and characteristics of structural elements (e.g., inner rings and outer rims, central peaks, stratigraphic uplift). In some cases this can be explained by post-impact modifications like erosion and tectonic adjustment (e.g., Gosses Bluff, Australia; Milton et al., 1972). In order to focus upon differences caused by

varying target conditions, we compare Ries crater with the two youngest and most pristine complex crater structures of Earth's impact record: the 0.87 Ma Zhamanshin crater, Kazakhstan (Masaitis et al., 1985), and the 1.07 Ma Bosumtwi crater in Ghana (Koeberl et al., 1997). Examples of topographic profiles are given in Figure 11. Both structures are believed to be well preserved and it is unlikely that any morphological differences can be explained by variations in the extent of erosion (Garvin and Schnetzler, 1994). The apparent diameter of Zhamanshin is ~14 km. The crater is located in a semi-desert, featuring a sedimentary platform environment with a typical erosion and infill amount of 0.02 mm/yr (Masaitis et al., 1985). For the 10.5 km (diameter of most pronounced morphological annular ring) Bosumtwi crater, which was formed on an equatorial crystalline shield region, the erosion rate is estimated to be slightly higher, between 0.06 and 0.14 mm/yr (Garvin and Schnetzler, 1994). In both cases, the quoted size of the structure refers to the most noticeable annular elevation, which is not necessarily equivalent to the real size of the crater. Therefore, we use the terminology "apparent crater rim" or "diameter" since it is not clear whether we compare similar structural elements. We believe that in the case of Bosumtwi and Zhamanshin, the apparent crater rim represents a similar structural element as the inner ring at Ries, which is ~12 km in diameter and almost the same size. As the inner ring structure of Ries is assigned to the approximate size of the transient cavity, we assume that the crater rims of Bosumtwi and Zhamanshin are roughly coincident with the size of the former transient cavity as well. Therefore, we affirm that all three craters are comparable in size. This idea is generally supported by the fact that the diameter of the transient cavity is an appropriate measure for the amount of impact energy, and in previous numerical models of the formation of Bosumtwi crater, the assumed amount of impact energy (750 m projectile) is in the same range as used in this study for the Ries models (Karp et al., 2003, 2004).

We note that the definition of crater size, especially for the size range of craters addressed in the present work, appears sometimes confusing. The Ries crater exhibits a well defined zone of normal faulting marking the maximum extent of the structure (classical definition of diameter D = 24 km) and a less morphologically pronounced inner ring that is assigned to the size of the transient cavity (D_t = 12 km). In contrast, Bosumtwi does not show clear evidence for an outer tectonic rim; hence, the diameter of the structure is indicated by the apparent crater rim. However, some clues exist for the presence of an outer ridge at a radius of 8–10.5 km defined by subtle topography (Wagner et al., 2002), which may be the equivalent of the tectonic rim at Ries. Note that in the case of Ries, the topographic elevation of the crystalline ring is widely obliterated by erosion and does not represent the dominating morphological element of the crater structure. Nevertheless, for the purpose of crater comparison, we use the diameter D_t of the inner ring structure because of the similar size of equivalent structural elements (assumed approximate size of transient cavity) in all three examples.

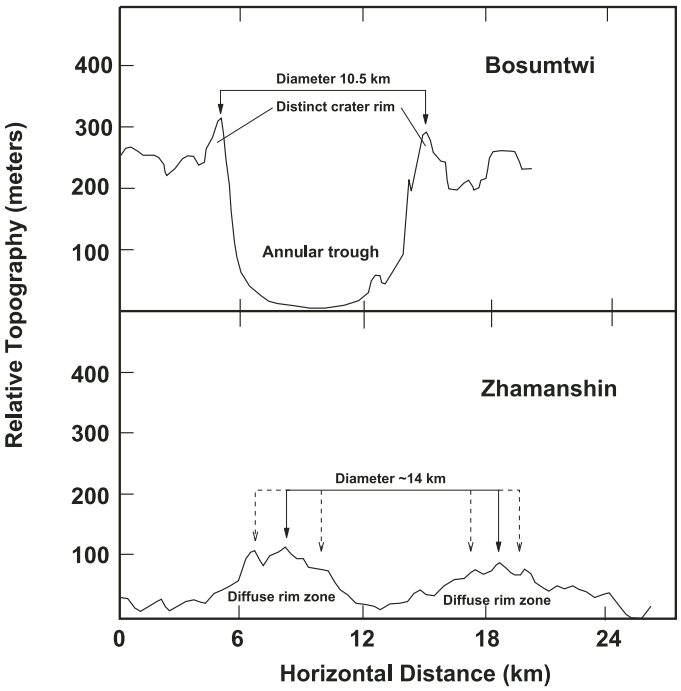

Figure 11. Topographic profiles through the centers of Bosumtwi and Zhamanshin, out to a distance of two radii from the crater rim crest. Morphometric values used in the text were derived from a large number of profiles through the craters (after Garvin and Schnetzler, 1994).

The most distinguishing feature between the three crater structures is the fact that the morphology of Zhamanshin appears to be much smoother, lacking clear, superficial crater-like topographic expressions. The aspect ratio (depth/diameter, where depth d as measured from the rim crest to the apparent crater floor) is d/D_t = 0.013, given by Garvin and Schnetzler (1994), and is based on the remote sensing signature. In contrast, Bosumtwi exhibits a well defined U-shape morphology with a steep-sided rim. Recent seismic reflection data identify a small peak structure in the center of the crater (Karp et al., 2002; Scholz et al., 2002). The aspect ratio is 0.048 (d/D_t = 0.5/10.5), where the depth is measured to the top of the breccia and melt layer. Based on remote sensing data, Garvin and Schnetzler (1994) specify a value of d/D_t = 0.029 for Bosumtwi, without, however, taking into account the thickness of the lake sediments (post-impact infill amount) in the crater. The higher erosional level of Ries crater allows only an approximation of the original crater depth by considering the thickness of the lake sediments (max 350 m; Ernstson, 1974) and an estimation of the former rim crest height. In order to determine a more sophisticated value for the depth of the Ries crater, we utilize empirical equations (scaling laws) that are based on the morphometry of selected (low erosional level) terrestrial complex craters. Grieve and Pesonen (1992) suggest two different relationships for crater depth as a function of diameter in sedimentary and crystalline targets:

$$d = 0.12\ D^{0.30} = 0.311 \text{ km (sedimentary)} \quad (1)$$

and

$$d = 0.15\ D^{0.43} = 0.588 \text{ km (crystalline)}, \quad (2)$$

where D is the diameter of the outer tectonic rim of Ries (D = 24 km). Although the sedimentary layer may have had an influence on the formation of the crater structure, the Ries crater was formed in a mainly crystalline target. Therefore, the aspect ratio for Ries is 0.049 (d/D_t; d = 0.588 km, D_t = 12 km). This value is in agreement with the observed depth/diameter ratio for Bosumtwi (d/D_t = 0.048). The differences in crater morphometry between Ries and Bosumtwi craters are mainly the existence of a more pronounced megablock zone adjacent to the inner basin and a less distinct topographic expression of the inner ring at Ries, which can be explained. Whereas the latter is most likely due to the higher amount of erosion at Ries, we believe that normal faulting at Ries (megablock zone) might have been caused by the weaker material properties of the overlying sediments, which support slumping into the crater cavity as the models in the previous section ("Numerical Modeling of Crater Formation") show (cf. Fig. 9). In comparison, Zhamanshin is unusually flat (aspect ratio d/D_t = 0.013), and Garvin and Schnetzler (1994) suggest this might be a consequence of weak or water-saturated target materials. Our model in Figure 9 confirms that a weak target causes craters having a smaller aspect ratio.

Ries and Bosumtwi formed under more or less comparable conditions with only slight differences in impact energy. As their aspect ratios are quite similar, one would expect their subsurface structure to be similar, too. In both cases, the crater basin is covered by a breccia or suevite layer. The thickness of this layer has a maximum extent of 300–400 m at Ries (Pohl et al., 1977) and 400–600 m at Bosumtwi (Karp et al., 2002). At Bosumtwi, it is uncertain whether the central peak structure is formed from breccia or whether it is actually structurally uplifted crystalline basement. Ries shows some clues for structural uplift underneath the crater but no topographic evidence for a central peak structure. In both craters, seismic investigations reveal similar P-wave velocities of 3–3.4 km s^{-1} in the brecciated layer (Angenheister and Pohl, 1976; Karp et al., 2002). Velocity models of greater depths are not yet available for Bosumtwi crater.

At first view, all three examples of complex craters discussed in this section look dissimilar in terms of crater morphology. But despite their differences in shape, Ries and Bosumtwi show a strong degree of resemblance due to their comparable (apparent) diameter (transient cavity), estimated aspect ratios, and target compositions. We believe that both craters are typical examples of small to middle-sized complex crater structures, and despite the lack of any obvious central elevation both craters are most similar to the type of central peak craters. For this reason, they represent appropriate natural laboratories on Earth, allowing the exploration of the crater formation processes.

SUMMARY AND CONCLUSIONS

The shape and structure of middle-sized complex impact craters on Earth vary considerably, and it is difficult to define characteristic topographic and structural elements. The numerical models of the formation of Ries crater show that the final crater shape is very sensitive to the constitutive properties of the target rocks. Sedimentary material is assumed to be less resistant against shear failure than crystalline basement rocks. For this reason, craters formed in sedimentary target compositions are relatively flat, whereas craters in mainly crystalline rocks exhibit more pronounced structural elements. This is demonstrated by the numerical models as well as by the comparison of the present morphology of Zhamanshin, Bosumtwi, and Ries craters, which were all formed by similarly energetic impacts. In the present study, we have used the diameter of the transient crater, which can be approximated by the extent of the inner most topographic elevation (inner ring or rim) in the three given examples, as a measure for crater size (or impact energy). The outermost ridge is usually used to determine the diameter of an impact structure, but as exemplified for Bosumtwi and Ries, this definition can cause a wrong assessment of the crater size.

The numerical models show that the crater morphology is highly sensitive to the strength profile of the near-surface rocks and the fluidization state of the rocks (acoustic fluidization parameters) during crater formation. In this respect, a similar amount of impact energy can cause different degrees of rim collapse and structural uplift. Accordingly, we propose that Ries and Bosumtwi are similarly sized craters and the inner ring structure of Ries is equivalent to the (interpreted) apparent crater rim at Bosumtwi. The presence of a sedimentary layer overlying crystalline basement at Ries might have supported the formation of a more pronounced megablock zone, which is more or less lacking at Bosumtwi.

Apart from matching the surface structure, our model for the formation of the Ries crater is also consistent with the subsurface observations. The structural uplift in the numerical model is ~1.5–2 km under the crater center and thus is consistent with our interpretation of the seismic refraction experiments. An estimate of the fragmentation zone beneath the crater based on the intensity of material movements in the dynamic model correlates with the anomalously high conductivity to a depth of 2 km due to interconnected brine-filled pores and fractures revealed by our magnetotelluric study and reduced seismic velocities to approximately the same depth. Gravity modeling in previous studies also showed that the observed mass deficit could be located entirely in the upper 2 km. Furthermore, the dynamic model gives evidence for molten material in the upper 300–500 m beneath the crater floor, which can be related to the suevite layer underneath the lake sediments detected by drilling and geoelectrical depth soundings. We conclude that the presented model agrees well with the observed crater morphometry and subsurface structure.

We should note, however, that our interpretation of the geophysical signature is not unique; in particular, it is not consistent

with previous studies. For example, Pohl et al. (1977) proposed that the observed gravity low is caused by a hemispherical fragmentation zone beneath the crater up to a depth of ~5 km, which is the reason for reduced seismic P-wave velocities to similar depth. This interpretation would be consistent with one of our models of the electrical conductivity distribution (model II, Fig. 5). However, our new interpretation is mainly based on our well-supported MT model of the electrical conductivity beneath the crater, which is in sound agreement with our reinterpreted velocity data and the early gravity models by Kahle (1969). Therefore, we support the assumption of a high degree of fracturing induced by release from shock pressure and plastic deformation remaining in the upper ~2 km, causing the observed reduced seismic velocities, the gravity low, and likewise the increased electrical conductivity. Below this level, basement rocks are uplifted by ~1–1.5 km, giving rise to increased seismic velocities in this area.

The numerical models show that both fragmentation and structural uplift of dense basement material accompanied the formation of the Ries crater. Hence, the geophysical signatures of both processes are superimposed. Different models of the subsurface, however, especially of the extent of the fragmentation zone, may be possible, and the present geophysical observations cannot constrain one unique model clearly.

ACKNOWLEDGMENTS

We are very grateful to the Deutsche Forschungsgemeinschaft (DFG) providing Kai Wünnemann with a scholarship to stay at Imperial College London, making the collaboration with J. Morgan possible (DFG gran Wu 355/3-1). The authors thank J. Pohl for providing the seismic reflection data and supporting us with valuable information on the Ries crater. Furthermore we appreciate the support by A. Jording during the magnetotelluric field campaigns and his assistance in processing the acquired data. The electromagnetic measurements were supported by the DFG-Graduiertenkolleg “Entstehung und Entwicklung des Sonnensystems” of the Deutsche Forschungsgemeinschaft. We are also very thankful to E. Turtle and F. Tsikalas for the very valuable and helpful review of the manuscript. Finally, we want to thank A. Deutsch for his great support editing the paper.

REFERENCES CITED

Amsden, A.A., Ruppel, H.M., and Hirt, C.W., 1980, SALE: A simplified ALE computer program for fluid flows at all speeds: LA-8095 Report: Los Alamos, NM, Los Alamos National Laboratories, 101 p.

Angenheister, G., and Pohl, J., 1969, Die seismischen Messungen im Ries von 1948–1969: Geologica Bavarica, v. 61, p. 304–326.

Angenheister, G., and Pohl, J., 1976, Results of seismic investigation in the Ries crater area (Southern Germany), *in* Giese, P., Prodehl, C., and Stein, A., eds., Explosion Seismology in Central Europe; Data and Results: Berlin, Springer-Verlag, p. 290–302.

Artemieva, N., Pierazzo, E., and Stöffler, D., 2002, Numerical modeling of tektite origin in oblique impacts: Implication to Ries-Moldavites strewn field: Bulletin of the Czech Geological Survey, v. 77, p. 31–39.

Bahr, K., 1991, Geological noise in magnetotelluric data: A classification of distortion types: Physics of the Earth and Planetary Interiors, v. 66, p. 24–38, doi: 10.1016/0031-9201(91)90101-M.

Bayerisches Geologisches Landesamt, 1999, Geologie des Rieses: München, Roland Eichborn Verlag, CD-ROM.

Birch, F., 1961, The velocity of compressional waves in rocks to 10 kilobars (Part II): Journal of Geophysical Research, v. 66, p. 2199–2224.

Blohm, E.-K., Friedrich, H., and Homilius, J., 1977, Ein Ries-Profil nach geoelektrischen Tiefensondierungen: Geologica Bavarica, v. 75, p. 381–393.

Bolten, R., and Müller, D., 1969, Das Tertiär im Nördlinger Ries und in seiner: Umgebung: Geologica Bavarica, v. 61, p. 87–130.

Christensen, N.I., and Mooney, W.D., 1995, Seismic velocity structure and composition of the continental crust: A global view: Journal of Geophysical Research, v. 100, B7, p. 9761–9788.

Collins, G.S., Melosh, H.J., Morgan, J.V., and Warner, M.R., 2002, Hydrocode simulations of Chicxulub Crater collapse and peak-ring formation: Icarus, v. 157, p. 24–33, doi: 10.1006/ICAR.2002.6822.

Ernstson, K., 1974, The structure of the Ries crater from geoelectric depth soundings: Journal of Geophysics, v. 40, p. 639–659.

Ernstson, K., and Pohl, J., 1974, Einige Kommentare zu den bohrlochgeophysikalischen Messungen in der Forschungsbohrung Nördlingen 1973: Geologica Bavarica, v. 72, p. 81–90.

Ernstson, K., and Pohl, J., 1977, Neue Modelle zur Verteilung der Dichte und Geschwindigkeit im Ries-Krater: Geologica Bavarica, v. 75, p. 355–371.

ERCEUGT-Group, 1992, An electrical resistivity crustal section from the Alps to the Baltic Sea (central segment of the EGT): Tectonophysics, v. 207, p. 123–139, doi: 10.1016/0040-1951(92)90474-K.

Fowler, S.R., White, R.S., Spence, G.D., and Westbrook, G.K., 1989, The Hatton Bank continental margin: Deep structure from two-ship expanding spread seismic profiles: Geophysical Journal, v. 96, p. 295–309.

Garvin, J.B., and Schnetzler, C.C., 1994, The Zhamanshin impact feature: A new class of complex craters? *in* Dressler, B.O., Grieve, R.A.F., and Sharpton, V.L., eds., Large Meteorite Impacts and Planetary Evolution: Geological Society of America Special Paper 293, p. 249–257.

Gentner, W., Lippolt, H.J., and Schaeffer, O.A., 1963, Argonbestimmung an Kaliumminералien-XI. Die Kalium-Argon-Alter der Gläser des Nördlinger Rieses und der böhmischmährischen Tektite: Geochimica et Cosmochimica Acta, v. 27, p. 191–200, doi: 10.1016/0016-7037(63)90058-9.

Grieve, R.A.F., and Pesonen, L.J., 1992, The terrestrial impact cratering record: Tectonophysics, v. 216, p. 1–30, doi: 10.1016/0040-1951(92)90152-V.

Grieve, R.A.F., Langenhorst, F., Stöffler, D., 1996, Shock metamorphism of quartz in nature and experiment: II Significance in geoscience: Meteoritics and Planetary Science, v. 31, p. 6–35.

Haak, V., Berktold, A., Wiesner, H., Knödel, K., and Rodemann, H., 1977, Zur Verteilung der elektrischen Leitfähigkeit im Ries, ermittelt aus Magneto-Tellurik-Messungen: Geologica Bavarica, v. 75, p. 395–400.

Ivanov, B.A., and Artemieva, N.A., 2002, Numerical modeling of the formation of large impact craters, *in* Koeberl, C., and MacLeod, K., eds., Catastrophic events and mass extinctions: Impact and beyond: Geological Society of America Special Paper 356, p. 619–629.

Ivanov, B.A., Kocharyan, G.G., Kostuchenko, V.N., and Kirjakov, A.F., and Pevzner, L., 1996, Puchezh Katunki impact crater: Preliminary data on recovered core block structure*:* Lunar and Planetary Science Conference XXVI, Houston, Texas, Abstract 1655, p. 589.

Ivanov, B.A., Deniem, D., and Neukum, G., 1997, Implementation of dynamic strength models into 2D hydrocodes: Application for atmospheric breakup and impact cratering: International Journal of Impact Engineering, v. 17, p. 375–386.

Jording, A., Ferrari, L., Arzate, J., and Jödicke, H., 2000, Crustal variations and terrane boundaries in southern Mexico as imaged by magnetotelluric transfer functions: Tectonophysics, v. 327, p. 1–13, doi: 10.1016/S0040-1951(00)00166-9.

Jung, K., and Schaaf, H., 1967, Gravimetermessungen im Nördlinger Ries und seiner Umgebung, Abschätzung der gesamten Defizitmasse: Zeitschrift für Geophysik, v. 33, p. 319–345.

Kahle, H.-G., 1969, Abschätzung der Störmasse im Nördlinger Ries: Zeitschrift für Geophysik, v. 35, p. 317–345.

Kahle, H.-G., 1970, Deutung der Schwereanomalie im Nördlinger Ries: Zeitschrift für Geophysik, v. 36, p. 601–606.

Karp, T., Milkereit, B., Janle, P., Danuor, K.S., Pohl, J., Berckhemer, H., and Scholz, C.A., 2002, Seismic investigation of the Lake Bosumtwi impact crater: preliminary results: Planetary and Space Science, v. 50, p. 735–743, doi: 10.1016/S0032-0633(02)00049-1.

Karp, T., Artemieva, N.A., and Milkereit, B., 2003, Seismic investigation and numerical modeling of the lake Bosumtwi impact crater: Conference on

"Impact Cratering: Bridging the Gap between Modeling and Observations," Houston, Texas, February 2003: Lunar and Planetary Institute, Abstract 1155, p. 42.

Karp, T., Artemieva, N.A., and Milkereit, B., 2004, Pre-drilling investigation of the lake Bosumtwi impact crater: Constrains from geophysical and numerical modeling: Lunar and Planetary Science Conference XXXV, Houston, Texas, March 2003, Abstract no. 1282.

Kocharyan, G.G., Kostuchenko, V.N., and Ivanov, B.A., 1996, Mechanics of rock massive disruption: Implementation to planetary cratering process: Lunar and Planetary Science Conference XXVI, Houston, Texas, March 1996, Abstracts, p. 677–678.

Koeberl, C., Bottomley, R., Glass, B.P., and Storzer, D., 1997, Geochemistry and age of Ivory Coast tektites and microtektites: Geochimica et Cosmochimica Acta, v. 61, p. 1745–1772, doi: 10.1016/S0016-7037(97)00026-4.

Mackie, R., Rieven, S., and Rodi, W., 1997, Users manual and software documentation for two-dimensional inversion of magnetotelluric data: Cambridge, Massachusetts, Massachusetts Institute of Technology, Earth Resources Laboratory, 14 p.

Mareschal, M., and Chouteau, M., 1990, A magnetotelluric investigation of the structural geology beneath Charlevoix crater, Quebec: Physics of the Earth and Planetary Interiors, v. 60, p. 120–131, doi: 10.1016/0031-9201(90)90254-U.

Masaitis, V.L., Mashchak, M.S., and Yezerskiy, V., 1985, Lifetime of impact features under different geologic conditions: Izvestia Academii Nauk SSSR, Seriya Geology, v. 2, p. 109–114.

Melosh, H.J., 1979, Acoustic fluidization: A new geologic process?: Journal of Geophysical Research, v. 84, p. 7513–7520.

Melosh, H.J., 1989, Impact cratering: A geological process: New York, Oxford University Press, 245 p.

Melosh, H.J., and Ivanov, B.A., 1999, Impact crater collapse: Annual Review of Earth and Planetary Science, v. 27, p. 385–415, doi: 10.1146/ANNUREV.EARTH.27.1.385.

Milton, D.J., Barlow, B.C., Brett, R., Brown, A.R., Glikson, A.Y., Manwaring, E.A., Moss, F.J., Sedmik, E.C.E., Van-Son, J., and Young, G.A., 1972, Gosses Bluff structure, Australia: Science, v. 175, p. 1199–1207.

Morgan, J.V., Warner, M.R., and Grieve, R.A.F., 2002, Geophysical constraints on the size and structure of the Chicxulub impact crater, *in* Koeberl, C., and MacLeod, K., eds., Catastrophic events and mass extinctions: Impact and beyond*:* Geological Society of America Special Paper 356, p. 39–46.

O'Keefe, J.D., and Ahrens, T.J., 1994, Impact induced melting on planetary surfaces, *in* Dressler, B.O., Grieve, R.A.F., Sharpton, V.L., eds., Large Meteorite Impacts and Planetary Evolution: Geological Society of America Special Paper 293, p. 103–109.

Pierazzo, E., Vickery, A.M., and Melosh, H.J., 1997, A reevaluation of impact melt production: Icarus, v. 127, p. 408–423, doi: 10.1006/ICAR.1997.5713.

Pilkington, M., and Grieve, R.A.F., 1992, The geophysical signature of terrestrial impact craters: Reviews of Geophysics, v. 30, p. 161–181.

Pohl, J., and Will, M., 1974, Vergleich der Geschwindigkeitsmessungen im Bohrloch der Forschungsbohrung Nördlingen 1973 mit seismischen Tiefensondierungen innerhalb und außerhalb des Ries: Geologica Bavarica, v. 72, p. 75–80.

Pohl, J., Stöffler, D., Gall, H., and Ernstson K., 1977, The Ries impact crater, *in* Roddy, D.J., Pepin, R.O., and Merrill, R.B., eds., Impact and explosion cratering: New York, Pergamon Press, p. 343–404.

Scholz, C.A., Karp, T., Milkereit, B., Amoako, P.Y.O., and Arko, J.A., 2002, Pronounced central uplift identified in the Bosumtwi impact structure, Ghana, using multichannel seismic reflection data: Geology, v. 30, p. 939–942, doi: 10.1130/0091-7613(2002)0302.0.CO;2.

Shoemaker, E.M., and Chao, E.C.T., 1961, New evidence for the impact origin of the Ries Basin, Bavaria, Germany: Journal of Geophysical Research, v. 66, p. 3371–3378.

Shuvalov, V., Dypvik, H., and Tsikalas, F., 2002, Numerical simulation of the Mjolnir marine impact crater: Journal of Geophysical Research, v. 107, doi: 10.1029/2001JE001698.

Stöffler, D., Artemieva, N.A., Pierazzo, E., and Ivanov, B.A., 2001, Ries crater Germany: Geology and numerical modeling of impact cratering [abs.]: Meteoritics and Planetary Science, v. 36, Supplement, p. A199.

Thompson, S.L., and Lauson, H.S., 1972, Improvements in the Chart D radiation-hydrodynamic code 3: Revised analytic equation of state: Report SC-RR-71 0714: Albuquerque, New Mexico, Sandia Laboratories, 119 p.

Tillotson, J.M., 1962, Metallic equation of state for hypervelocity impact: General Atomic Report GA-3216: San Diego, Advanced Research Project Agency, 141 p.

Wagner, R., Reimold, W.U., and Brandt, D., 2002, Bosumtwi impact crater Ghana: A remote sensing investigation, *in* Plado, J., and Pesonen, L.J., eds., Meteorite impacts in Precambrian shields: Berlin, Springer-Verlag, 336 p.

Wünnemann, K., and Ivanov, B.A., 2003, Numerical modeling of the impact crater depth-diameter dependence in an acoustically fluidized target: Planetary and Space Science, v. 51, p. 831–845, doi: 10.1016/J.PSS.2003.08.001.

Wünnemann, K., and Lange, M.A., 2002, Numerical modeling of impact induced modifications of the deep-sea floor: Deep-Sea Research II, v. 49, p. 969–981.

Zelt, C.A., 1998, Lateral velocity resolution from three-dimensional seismic refraction data: Geophysical Journal International, v. 135, p. 1101–1112, doi: 10.1046/J.1365-246X.1998.00695.X.

Zelt, C.A., and Smith, R.B., 1992, Seismic travel-time inversion for 2D crustal velocity structures: Geophysical Journal International, v. 108, p. 16–34.

Zhang, P., Rasmussen, T.M., and Pederson, L.B., 1988, Electric resistivity structure of the Siljan impact region: Journal of Geophysical Research, v. 93, p. 6485–6501.

Manuscript Accepted by the Society 9 August 2004

Geological Society of America Special Papers

Is Ries crater typical for its size? An analysis based upon old and new geophysical data and numerical modeling

K. Wünnemann, J.V. Morgan and H. Jödicke

Geological Society of America Special Papers 2005;384; 67-83
doi:10.1130/0-8137-2384-1.67

Notes